Springer

Dear Author:

Please find attached the final pdf file of your contribution, which can be viewed using the Acrobat Reader, version 3.0 or higher. We would kindly like to draw your attention to the fact that copyright law is also valid for electronic products. This means especially that:

- You may print the file and distribute it amongst your colleagues in the scientific community for scientific and/or personal use.

- You may make your article published by Springer-Verlag available on your personal home page provided the source of the published article is cited and Springer-Verlag and/or other owner is mentioned as copyright holder. You are requested to create a link to the published article in Springer's internet service. The link must be accompanied by the following text: "The original publication is available at springerlink.com". Please use the appropriate DOI for the article. Articles disseminated via SpringerLink are indexed, abstracted and referenced by many abstracting and information services, bibliographic networks, subscription agencies, library networks and consortia.

- Without having asked Springer-Verlag for a separate permission your institute/your company is not allowed to place this file on its homepage.

- You may not alter the pdf file, as changes to the published contribution are prohibited by copyright law.

- Please address any queries to the production editor of the journal in question, giving your name, the journal title, volume and first page number.

Yours sincerely,

Springer-Verlag

Journal of Geodesy (2003) 77: 493–502
DOI 10.1007/s00190-003-0336-3

Journal of Geodesy

Applying differential InSAR to orbital dynamics: a new approach for estimating ERS trajectories

A.O. Kohlhase[1], K.L. Feigl[1], D. Massonnet[2]

[1] Department of Terrestrial and Planetary Dynamics, Centre National de la Recherche Scientifique, 14 Avenue E. Belin, 31400 Toulouse, France; e-mail: kurt.feigl@cnes.fr; Tel.: +33-5-61-33-29-40; Fax: +33-5-61-33-29-00
[2] Department of Management and Acquisition, Centre National d'Etudes Spatiales, 18 Avenue E. Belin, 31055 Toulouse, France e-mail: didier.massonnet@cnes.fr; Tel.: +33-5-61-27-34-18; Fax: +33-5-61-28-28-99

Received: 16 April 2002 / Accepted: 26 March 2003

Abstract. A new approach for tuning the trajectories of the European remote sensing (ERS) satellites is developed and assessed. Differential dual-pass interferometry is applied to calculate interferograms from the phase difference of synthetic aperture radar (SAR) images acquired by the ERS satellites over the site of the 1992 earthquake in Landers, California. These interferograms contain information about orbital trajectories and geophysical deformation. Beginning with good prior estimates of the orbital trajectories, a radial and an across-track orbital adjustment is estimated at each epoch. The data are the fringe counts along distance and azimuth. Errors in the across-track and radial components of the orbit estimates produce fringes in the interferograms. The spacing between roughly parallel fringes gives the gradients in distance and azimuth coordinates. The approach eliminates these fringes from interferometric pairs spanning relatively short time intervals containing few topographic residuals or atmospheric artefacts. An optimum interferometric path with six SAR acquisitions is selected to study post- and inter-seismic deformation fields. In order to regularize the problem, it is assumed that the radial and across-track adjustments both sum to zero. Applying the adjustment approach to the prior estimates of trajectory from the Delft Institute for Earth-Orientated Space Research (DEOS), root mean squares of 7.3 cm for the across-track correction components and 2.4 cm for the radial ones are found. Assuming 0.1 fringes for the a priori standard deviation of the measurement, the approach yields mean standard deviations of 2.4 cm for the across-track and 4.5 cm for the radial components. The approach allows an 'interval by interval' improvement of a set of orbital estimates from which post-fit interferograms of different time intervals spanning a total 3.8-year inter-seismic time interval can be created. The interferograms calculated with the post-fit orbital estimates compare favorably with those corrected with a conventional orbital tuning approach. Using the adjustment approach, it is possible to distinguish between orbital and deformation contributions to interferometric SAR (InSAR) phase gradients. Surface deformation changes over an inter-seismic time interval longer than one year can be measured. This approach is, however, limited to well-correlated interferograms where it is possible to measure the fringe gradient.

Correspondence to: K.L. Feigl
A.O. Kohlhase now at:
Microwaves and Radar Institute, Deutsches Zentrum für Luft- und Raumfahrt e.V., Münchner Straße 20, 82234 Weßling, Germany.
e-mail: andreas.kohlhase@dlr.de
Tel.: +49-08153-28-2106
Fax: +49-08153-28-1449

1 Introduction

We consider the orbital contribution in differential interferometric synthetic aperture radar (InSAR) images. Since the phase difference between SAR images is acquired in similar geometric conditions, but at two different epochs, the resulting interference pattern shows fringes that represent contours of the change in range between the SAR antenna and the ground point. If we subtract the topographic contribution from the phase in each pixel, we obtain a so-called differential interferogram which records the deformation field. In practice, however, this measurement still contains contributions from topography and orbit uncertainties as well as atmospheric contributions.

Consequently, the usefulness of an interferogram is limited by the problem of distinguishing deformation signals from orbital uncertainties (Massonnet and Feigl 1998). The standard processing scheme assumes that errors in the satellite trajectories create a planar interference pattern with parallel fringes. Sometimes called a 'phase ramp', this pattern is indistinguishable from a crustal deformation field with constant fringe gradient.

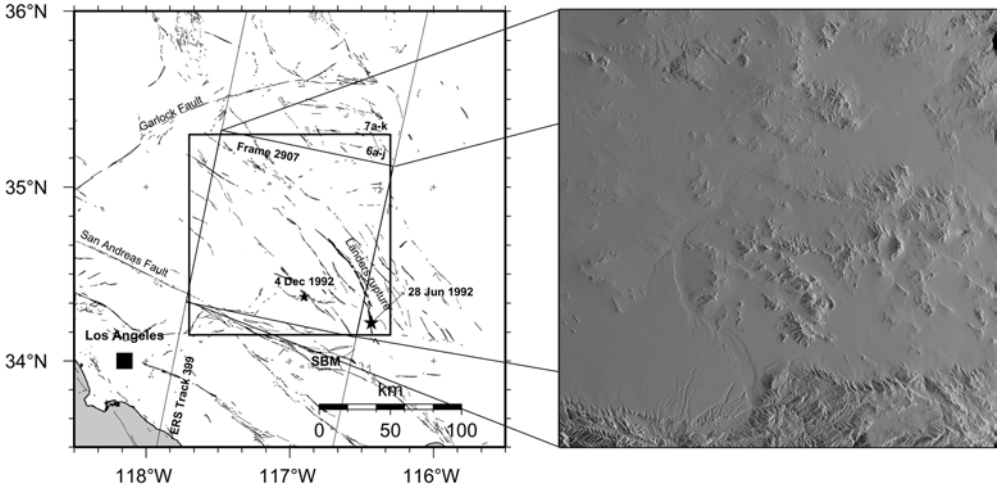

Fig. 1. Left side shows the location map of the study area around Landers in southern California. *Stars* indicate earthquake epicenters of the 28 June 1992 Landers ($M_L = 7.3$) main shock and the 4 December 1992 ($M_L = 5.1$) aftershock. The *box with bold lines* delimits the area of Fig. 7. The inclined frame 2907 on the ERS track 399 is our selected SAR scene and the area delimiting the interferograms of Fig. 6. Right side shows the simulated SAR backscatter (amplitude) image in radar geometry calculated with the 3 arcsec DEM and the prior estimate of orbit 20928

Currently, the best available estimates for ERS-1 and ERS-2 trajectories, based on the fully independent Delft gravity model (DGM)-E04 and the *GeoForschungsZentrum* (GFZ) PGM055, show root-mean-square (RMS) orbit differences of about 7 cm in the radial, 24 cm in the along-track, and 18 cm in the across-track directions (Scharroo and Visser 1998). These values should, in principle, be amenable to improvement by using the interferometric SAR phase change to measure range within a fraction of a 5.6-cm wavelength. In practice, however, our approach will work best for the radial and across-track components because of geometry. Previously, we have evaluated the relative quality of various orbital estimates by counting the number of fringes remaining in differenced interferograms. However, this approach works well only in cases where the orbital contribution dominates the error budget. In practice, this means one full 28-mm fringe over a 110-km-wide scene, or a proportional error of $\sim 3 \times 10^{-7}$. Orbital errors smaller than this value tend to drown in noise from other sources, such as tropospheric heterogeneities or unmodeled topographic relief. In this paper, we model the orbital errors and adjust the satellite trajectories in a quasi-absolute sense. Then we use the improved orbital estimates to calculate the interferograms again.

2 InSAR data selection

We select ERS data over the area shown in Fig. 1. Many acquisitions are available because of the interest in the 28 June 1992 Landers earthquake in California (Massonnet et al. 1993, 1994, 1996; Zebker et al. 1994; Peltzer et al. 1998). We have selected the 110 by 110-km-wide scene of frame 2907 in track 399 covering the area between the San Andreas Fault and the Landers rupture. The satellite has acquired an SAR image of this single scene during p different passes. The number of possible interferometric pairs, not counting autocorrelations or reversals, is

$$q = \frac{p(p-1)}{2}, \quad p \geq 2, \ p \in \mathbb{N} \tag{1}$$

However, the number of strictly independent pairs is only $p/2$. But such a minimal set of pairs does not provide any redundancy for identifying artefacts associted with a particular image (epoch), such as might occur under anomalous atmospheric conditions. To identify an epoch as anomolous, we should include it in at least two pairs. This leads to a basis set of pairs. Omitting the pair composed of the first and last epochs, we find the number of pairs in the basis set to be

$$k = p - 1 \tag{2}$$

This is the minimum number of pairs required to capture all the geophysical deformation between the epochs of the first and last images.

Of course, fringe counts in pairs sharing a common image are correlated. If, for example, an atmospheric anomaly contaminates the image acquired at the second epoch, an artefact will appear in two interferometric pairs (1, 2 and 2, 3) of the basis set. Our first step then, is to optimize the choice of the k best pairs among the q possibilities. We visualize our choice in Fig. 2. Figure 2A shows a conventional plot of baseline as a function of time. Figure 2B displays the same information in different way. It plots the time-ordered list of interferometric pairs as a path through a two-dimensional (2-D) space with two coordinates: accumulated timespan and accumulated baseline. To emphasize the optimal choice of interferometric pairs with respect to temporal and geometric decorrelation, this representation shows a 'good' path as including pairs with both (1) relatively short time intervals and (2) shallow slope.

Temporal decorrelation occurs when the arrangement of scatterers within a resolution cell or their electrical properties changes as a function of time between the first and the second data acquisition epochs (Hanssen 2001). Thus, interferometric pairs spanning shorter times are 'good' for measuring fringe gradients.

Geometric decorrelation occurs as the separation between the two orbital trajectories increases. The correlation coefficient is inversely proportional to the component $|B_\perp|$ of the orbital separation ('baseline') vector perpendicular to the range direction (see Fig. 5).

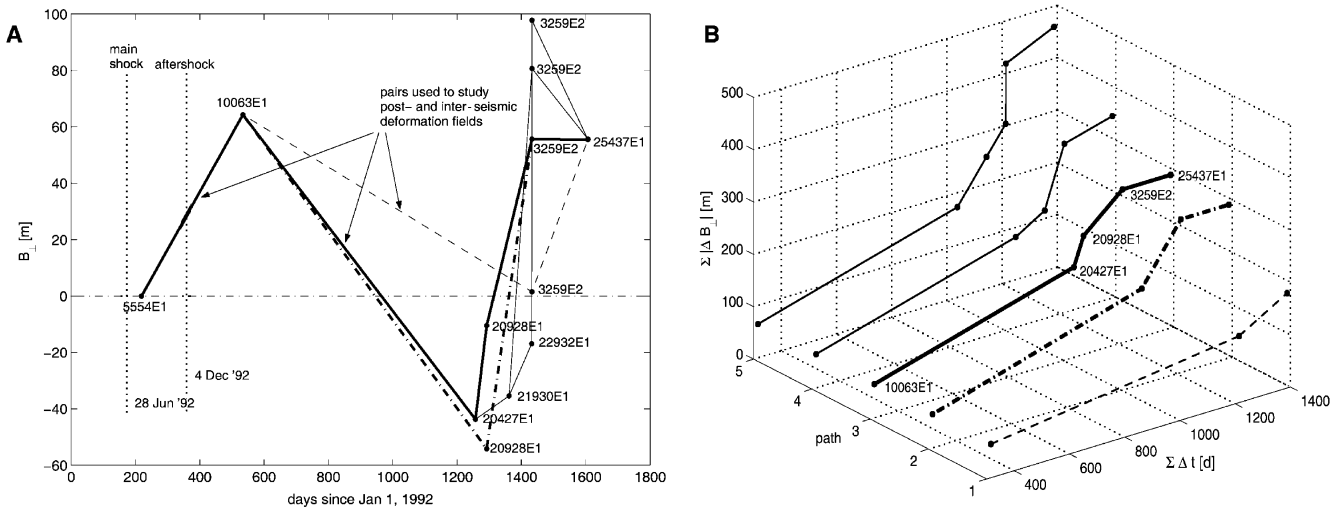

Fig. 2. **A** ERS SAR data set represented as perpendicular baseline component versus calendar time since 1 January 1992. For all these pairs, the altitude of ambiguity in absolute value is $|h_a| > 50$ m. Reference orbit is 5554E1. For the *solid line*, we find an optimal compromise between short $B_\perp$, short time intervals, number of interferometric pairs and the shortest interval bridging over the gap of SAR data at the end of 1993 and in 1994. The *dashed path* contains the pair with the longest time interval and is supposed to be calculated after the orbit adjustment with the improved estimates obtained from the optimum path. **B** Cumulative differences of $B_\perp$ in absolute value versus the cumulative time intervals and the path number. Although path 2 (*bold dashed-dotted line*) has the shallowest overall slope, it only includes three images. Instead, we choose path 3 (*solid line*) as the optimum because it includes four images and has the shortest time interval (20427E1, 10063E1) to bridge over the data gap beween 1993 and 1994

For interferometric pairs $|B_\perp|$ beyond a critical value, correlation vanishes because the spectral shift exceeds the pulse bandwidth (Gatelli et al. 1994). The value of $|B_\perp|$ is usually used to describe the sensitivity of an interferometric pair to topographic elevation. It is inversely proportional to the altitude of ambiguity h_a, the shift necessary to produce one topographic fringe, as defined by Massonnet and Rabaute (1993) and sketched by Massonnet and Feigl (1998). This implies that large values of $|h_a|$ or small values of $|B_\perp|$ increase the degree of geometric correlation and thereby the signal-to-noise ratio in the interferogram. Such values are 'good'. To minimize topographic effects in the interferograms, we have selected a relatively flat area with a precise digital elevation model (DEM) (Fig. 1). We use a digital terrain elevation data model of Level 1 (DTED-1) with 3-arcsec (~ 90 m) postings. The stated objective for its absolute vertical accuracy ε is "± 30 m linear error at 90% probability" (US Geological Survey 1993). Consequently, an error of ε meters in the DEM used for the topographic correction will create an artefactual phase change of ε/h_a fringe in the interferogram.

To exclude ground-deformation changes, we avoid co-seismic pairs spanning main shocks and pairs with long time intervals. We only list the interferometric pairs in chronological order such that the successive pairs share a common image. The total length of the series should also be as long as possible. These constraints restrict our choice to interferometric paths where all pairs have an altitude of ambiguity $|h_a| > 50$ m (Fig. 2A).

In order to find the optimum among the selected paths, we consider the accumulated differences of the vertical baseline components in absolute value of each path as a function of the accumulated time intervals (Fig. 2B). The optimum path should span a 14-month data gap in 1993–1994 and include a relatively large number of pairs. Our optimal interferometric path contains $p = 6$ acquisition epochs. It constitutes our basis set of $k = 5$ pairs chosen among the $q = 15$ possibilities. Table 1 summarizes the main parameters for each interferometric pair of this path. Since the worst pair in the optimial path has $|h_a| = 120$ m, we expect phase errors smaller than 1/4 fringe from topography.

3 Orbit errors

An orbital error vector is usually expressed in the coordinate system rotating with the satellite and consists of three components: the along-track, the across-track and the radial component, as sketched in Fig. 3A. Since an interferogram is a relative measure, the resulting error of the first and second orbit at a certain time is represented by the baseline error vector **n** (Fig. 4B) that contributes to the phase error in the interferogram (Hanssen 2001). The error causes an interference pattern that we call orbital fringes. They tend to have a constant gradient in a certain direction. In other words, the

Table 1. Interferometric parameters of the five pairs of our optimal path. The parameters were calculated from the DEOS prior orbit estimates. The altitude of ambiguity h_a refers to the NR pixel at t_0

Pair	Orbit	Numbers	Δt (d)	h_a (m)
2, 1	10063E1	5554E1	315	−119.3
3, 2	20427E1	10063E1	723	175.0
4, 3	20928E1	20427E1	35	795.2
5, 4	3259E2	20928E1	141	−131.5
6, 5	25437E1	3259E2	174	−154.4

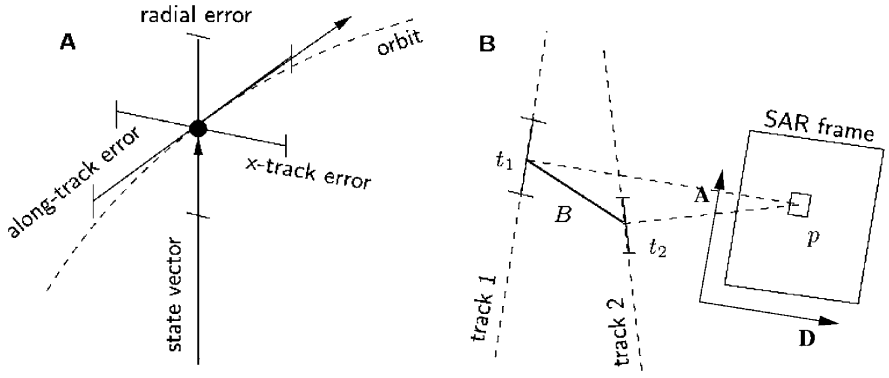

Fig. 3. **A** Three-dimensional sketch of the along-track, across-track and radial error bars. **B** Top view of two converging tracks. Resolution element p is observed at ($t = t_1$) from the first track 1, and at ($t = t_2$) from the repeat track 2. The along-track error is indicated by the error bars along the track, (from Hanssen 2001)

number of fringes per unit distance does not vary much over a scene.

For SAR interferometry, along-track errors are usually accounted for during the co-registration of the two SAR images (Hanssen 2001) see Fig. 3B. They can also be regarded as timing errors (Massonnet and Vadon 1995). Consequently, only the radial and across-track errors propagate into the interferogram, making the problem 2-D. Errors in radial and across-track components both produce orbital fringes parallel to the track. The fringes perpendicular to the track reveal a variation of the previous ones or, in other terms, an incorrect estimate of the radial and across-track velocities. For correction purposes, it is sufficient to measure orbital fringes in the radar geometry, that is along distance **D** and azimuth **A** coordinates prior to geocoding (Fig. 3B). To obtain the fringe gradient in **D** direction, we count the relative number of fringes along distance between the near-range (NR) and far-range (FR) corners. Counting fringes perpendicular to the track between a point at the beginning of the SAR acquisition t_0 and the end of the acquisition t_e yields the fringe gradient in **A** direction. Note that the fringes are not necessarily parallel, so that the fringe gradient can vary between NR and FR and between t_0 and t_e. This phenomenon is caused by the baseline vector varying as a function of time during acquisition when the two tracks are diverging or converging, as illustrated in Fig. 4A. The measure is a dimensionless fringe count number for distance and azimuth. To obtain a distance, we multiply the fringe count by 28 mm, the half-wavelength of the ERS radars.

We want to evaluate the precise orbit products from DEOS which are frequently used for InSAR analysis. Of course, our approach also applies to the other ERS orbit producers such as the German Data Processing and Archiving Facility (D-PAF) or the restituted 'ORRM' orbits provided by the European Space Agency (ESA).

4 Virtual reference trajectory

An orbit error is the difference between a prior estimate of the actual or true state vector at a certain time and the actual state vector derived from precise orbit determination (POD). This error changes artefactually the satellite-to-ground distance and creates an artefactual phase signal in the interferogram. Mathematically, the actual state vector $\tilde{\mathbf{r}}$ at a certain time is the sum of the prior estimate $\mathbf{r}^{\text{prior}}$ and an adjustment vector $\delta\mathbf{r}$ to be estimated later.

$$\tilde{\mathbf{r}} = \mathbf{r}^{\text{prior}} + \delta\mathbf{r} \tag{3}$$

The relation between the adjustment vector $\delta\mathbf{r}$ and the interferometric error phase $\Delta\phi$ in a pixel is given by

$$\Delta\phi = \frac{4\pi}{\lambda}\delta\mathbf{r}\cdot\mathbf{s} \tag{4}$$

or

$$\Delta\rho = -\delta\mathbf{r}\cdot\mathbf{s} \tag{5}$$

where $\mathbf{s}$ is the unit vector pointing from the ground point toward the prior estimate of satellite position, λ the wavelength and $\Delta\rho$ the equivalent range change that would have been observed by the SAR antenna. The pointing vector $\mathbf{s}$ is dimensionless and defined as

$$\mathbf{s} = \frac{\boldsymbol{\rho}}{|\boldsymbol{\rho}|} \tag{6}$$

where $\boldsymbol{\rho}$ is the range vector from the ground to the satellite (Fig. 5). We write the adjustment vector as

$$\delta\mathbf{r}(t) = \mathbf{e}^{(n)}\delta y(t) + \mathbf{e}^{(r)}\delta z(t) \tag{7}$$

where $\delta y(t)$ (across-track) and $\delta z(t)$ (radial) are the time-dependent orbital correction parameters in the plane orthogonal to the trajectory. The unit vectors $\mathbf{e}^{(n)}$ and $\mathbf{e}^{(r)}$ are defined by

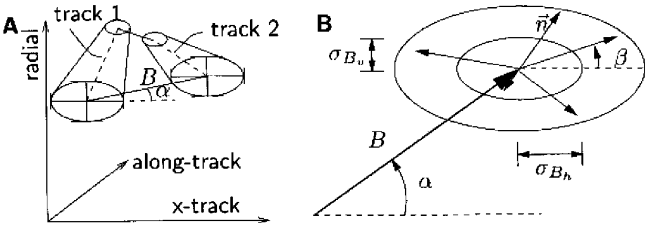

Fig. 4. **A** Quasi-3-D view of the two converging orbits causing a length change of the baseline vector **B** and its orientation angle α. The error ellipses are based on the radial and across-track errors. **B** The error vector **n**, defined by its length and orientation angle β, is situated somewhere within a confidence ellipse, from (Hanssen 2001)

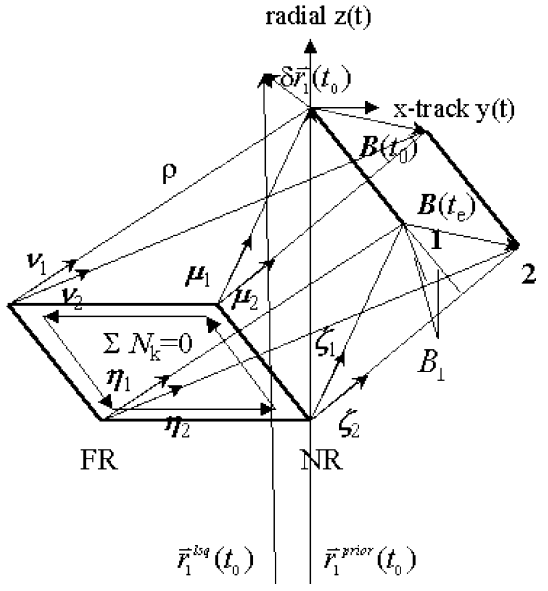

Fig. 5. Dual-pass and interferometric configuration for the four corners μ, ν, ζ, η and geometry of the prior state vector adjustment of orbit 1 at t_0. Note that the fringe count sum along the four sides must be zero

$$\mathbf{e}^{(n)} = \frac{\mathbf{r}\times\mathbf{v}}{|\mathbf{r}\times\mathbf{v}|} \quad \text{and} \quad \mathbf{e}^{(r)} = \frac{\mathbf{r}}{|\mathbf{r}|} \tag{8}$$

The (n) superscript indicates the direction normal to the plane spanned by the **r**- and **v**-vector and thus the across-track direction in the inertial Earth reference system. The (r) superscript denotes the radial direction. The velocity vector **v** of the satellite refers to the same epoch. Henceforth, we also express the adjustment vector in the inertial Earth reference system. To estimate the improved first and second (repeat) passes, we have to adjust the orbits in such a way that

$$\Delta(\delta\mathbf{r}_{12}) = \delta\mathbf{r}_1 - \delta\mathbf{r}_2 = (\tilde{\mathbf{r}}_1 - \mathbf{r}_1^{\text{prior}}) - (\tilde{\mathbf{r}}_2 - \mathbf{r}_2^{\text{prior}}) \tag{9}$$

Thus, $\delta\mathbf{r}_i$ is the adjustment of orbit i relative to the state vector $\tilde{\mathbf{r}}_i$ of the virtual reference trajectory. It yields the improved state vector of orbit i according to Eq. (3). A fringe count on an interferogram is always differential because it represents a change of range change between two distinct ground points. We write the orbital contribution to the range change as

$$\delta(\Delta\rho) = (\delta\mathbf{r}_1\cdot\mathbf{s}_1 - \delta\mathbf{r}_1\cdot\mathbf{w}_1) - (\delta\mathbf{r}_2\cdot\mathbf{s}_2 - \delta\mathbf{r}_2\cdot\mathbf{w}_2) \tag{10}$$

where $\mathbf{s}_i$ and $\mathbf{w}_i$ are the dimensionless unit vectors of the two targets pointing toward the satellite in track i. The data $\delta(\Delta\rho)$ measure the differential range change along the line between target s and w. We count fringes along distance and azimuth to estimate the orbit error components separately. Building the Jacobian matrix $\mathscr{J}_{\mathbf{s}}(y,z)$ with the vector equation, Eq. (7), yields

$$\mathscr{J}_{\mathbf{s}}(y,z) = \left(\frac{\partial\mathbf{r}}{\partial y}, \frac{\partial\mathbf{r}}{\partial z}\right) = (\mathbf{e}^{(n)}, \mathbf{e}^{(r)}) \tag{11}$$

This means that the partial derivatives with respect to the parameters δy and δz are the dimensionless unit vectors of the across-track and radial error components expressed in the Earth-fixed reference system. Consequently, the differential range change vector can be seperated into distance and azimuth components.

We can develop the relation for the differential range change $\delta_D(\Delta\rho)$ along distance (Fig. 5) to estimate the across-track error at t_0 by applying Eqs. (10) and (11)

$$\begin{aligned}\delta_{D_0}(\Delta\rho) &= \mathbf{e}_1^{(n)}(t_0)\delta y_1(t_0)(\boldsymbol{\nu}_1 - \boldsymbol{\mu}_1) \\ &\quad - \mathbf{e}_2^{(n)}(t_0)\delta y_2(t_0)(\boldsymbol{\nu}_2 - \boldsymbol{\mu}_2) \\ &= \begin{bmatrix}\mathbf{e}_1^{(n)}(t_0)\boldsymbol{\xi}_1 & -\mathbf{e}_2^{(n)}(t_0)\boldsymbol{\xi}_2\end{bmatrix}\begin{bmatrix}\delta y_1(t_0)\\ \delta y_2(t_0)\end{bmatrix}\end{aligned} \tag{12}$$

with

$$\boldsymbol{\xi}_i = \boldsymbol{\nu}_i - \boldsymbol{\mu}_i$$

At t_e we obtain

$$\begin{aligned}\delta_{De}(\Delta\rho) &= \mathbf{e}_2^{(n)}(t_e)\delta y_2(t_e)(\boldsymbol{\eta}_2 - \boldsymbol{\zeta}_2) \\ &\quad - \mathbf{e}_1^{(n)}(t_e)\delta y_1(t_e)(\boldsymbol{\eta}_1 - \boldsymbol{\zeta}_1) \\ &= \begin{bmatrix}-\mathbf{e}_1^{(n)}(t_e)\boldsymbol{\tau}_1 & \mathbf{e}_2^{(n)}(t_e)\boldsymbol{\tau}_2\end{bmatrix}\begin{bmatrix}\delta y_1(t_e)\\ \delta y_2(t_e)\end{bmatrix}\end{aligned} \tag{13}$$

with

$$\boldsymbol{\tau}_i = \boldsymbol{\eta}_i - \boldsymbol{\zeta}_i$$

where $\boldsymbol{\nu}$ and $\boldsymbol{\eta}$ are the dimensionless unit pointing vectors in the two corners at FR and $\boldsymbol{\mu}$ and $\boldsymbol{\zeta}$ are those at NR (see Fig. 5).

The same can be rewritten for orbit pairs $(3,2), (4,3)$, etc. Applying again Eqs. (10) and (11) to develop the relation for the change of range change $\delta_A(\Delta\rho)$ along azimuth to estimate the radial error at NR and FR yields

$$\begin{aligned}\delta_{A_{nr}}(\Delta\rho) &= \mathbf{e}_2^{(r)}(t_0)\delta z_2(t_0)\boldsymbol{\mu}_2 - \mathbf{e}_1^{(r)}(t_0)\delta z_1(t_0)\boldsymbol{\mu}_1 \\ &\quad - \mathbf{e}_2^{(r)}(t_e)\delta z_2(t_e)\boldsymbol{\zeta}_2 + \mathbf{e}_1^{(r)}(t_e)\delta z_1(t_e)\boldsymbol{\zeta}_1 \\ &= \begin{bmatrix}-\mathbf{e}_1^{(r)}(t_o)\boldsymbol{\mu}_1 & \mathbf{e}_2^{(r)}(t_o)\boldsymbol{\mu}_2 \\ \mathbf{e}_1^{(r)}(t_e)\boldsymbol{\zeta}_1 & -\mathbf{e}_2^{(r)}(t_e)\boldsymbol{\zeta}_2\end{bmatrix}\begin{bmatrix}\delta z_1(t_0)\\ \delta z_2(t_0)\\ \delta z_1(t_e)\\ \delta z_2(t_e)\end{bmatrix}\end{aligned} \tag{14}$$

and

$$\begin{aligned}\delta_{A_{fr}}(\Delta\rho) &= \mathbf{e}_1^{(r)}(t_0)\delta z_1(t_0)\boldsymbol{\nu}_1 - \mathbf{e}_2^{(r)}(t_0)\delta z_2(t_0)\boldsymbol{\nu}_2 \\ &\quad - \mathbf{e}_1^{(r)}(t_e)\delta z_1(t_e)\boldsymbol{\eta}_1 + \mathbf{e}_2^{(r)}(t_e)\delta z_2(t_e)\boldsymbol{\eta}_2 \\ &= \begin{bmatrix}\mathbf{e}_1^{(r)}(t_o)\boldsymbol{\nu}_1 & -\mathbf{e}_2^{(r)}(t_o)\boldsymbol{\nu}_2 \\ -\mathbf{e}_1^{(r)}(t_e)\boldsymbol{\eta}_1 & \mathbf{e}_2^{(r)}(t_e)\boldsymbol{\eta}_2\end{bmatrix}\begin{bmatrix}\delta z_1(t_0)\\ \delta z_2(t_0)\\ \delta z_1(t_e)\\ \delta z_2(t_e)\end{bmatrix}\end{aligned} \tag{15}$$

respectively. The same can be rewritten for the other pairs.

We seek to find the best linear unbiased orbital correction parameters $\delta y_i(t)$ and $\delta z_i(t)$ by solving the functional model equation

$$\mathbf{A}\mathbf{x} - \mathbf{d} = \boldsymbol{\epsilon}, \quad \mathbf{A} \in \mathbb{R}^{n\times m},\ \mathbf{x} \in \mathbb{R}^m,\ \mathbf{d}, \boldsymbol{\epsilon} \in \mathbb{R}^n \tag{16}$$

according to the Gauss–Markoff model definition (Koch 1999). The data vector $\mathbf{d}$ contains our measurement of fringe count. The residual vector $\boldsymbol{\epsilon}$ reflects the measurement errors with the expectation $E\{\boldsymbol{\epsilon}\} = 0$. The design matrix $\mathbf{A}$ contains elements according to Eqs. (12), (13), (14), and (15). The unknown parameter vector $\mathbf{x}$ contains the components $\delta y_i(t_0)$, $\delta y_i(t_e)$ or $\delta z_i(t_0)$, $\delta z_i(t_e)$. In accordance with the weighted least-squares (LS) orbit determination problem (Montenbruck and Gill 2000), the solution is given by the estimation

$$\mathbf{x}^{\text{lsq}} = (\mathbf{A}^T\mathbf{W}\mathbf{A})^{-1}\mathbf{A}^T\mathbf{W}\mathbf{d} \tag{17}$$

which indicates that the LS estimate $\mathbf{x}^{\text{lsq}}$ still differs from the true value of the parameter vector $\tilde{\mathbf{x}}$ in the presence of measurement errors. Thus we have

$$\delta\mathbf{r}_i^{\text{lsq}} = \mathbf{r}_i^{\text{lsq}} - \mathbf{r}_i^{\text{prior}}, \qquad \delta\mathbf{r}_i^{\text{lsq}} \subseteq \mathbf{x}^{\text{lsq}} \tag{18}$$

The $\delta\mathbf{r}_i^{\text{lsq}}$ estimate is a quasi-absolute adjustment of the prior state vector of orbit i at time t. The matrix $\mathbf{A}^T\mathbf{W}\mathbf{A} \in \mathbb{R}^{n\times n}$ must be symmetric and positive definite. The diagonal weighting matrix $\mathbf{W}$ contains the squared inversed measurement standard deviations $\sigma_1, \ldots, \sigma_n$. We apply Eq. (17) twice to estimate the across-track and radial component separately. For $p = 6$ acquisition epochs and the two times t_0 and t_e, we obtain $m = 2p = 12$ free parameters for each orbit component. Equations (12), (13), (14), and (15) yield in each case $n = 2(p-1) = 10$ linearly independent rows because of Eq. (1). Hence, we have a rank deficiency of $m - n = 12 - 10 = 2$ for each equation system.

To overcome this, we regularize the solution by constraining the sum of the adjustment components of the ith orbit to be zero such that

$$\sum_{i=1}^{p} \delta y_i(t_0), \delta y_i(t_e) = 0 \tag{19}$$

and

$$\sum_{i=1}^{p} \delta z_i(t_0), \delta z_i(t_e) = 0 \tag{20}$$

respectively. This adds two more equations to each system, bringing the problem to full rank and making the two equation systems uniquely solvable ($n = m = 12$). We solve them using a singular-value decomposition algorithm (Schwarz 1997).

Since we obtain two adjustment vectors $\delta\mathbf{r}(t_0)$ and $\delta\mathbf{r}(t_e)$ or four parameters for each acquisition, we can define two linear functions for each correction component

$$\delta y(t) = a_0 + a_1 \cdot t \qquad \text{and} \qquad \delta z(t) = b_0 + b_1 \cdot t \tag{21}$$

with

$$a_0 = \delta y(t_0), \qquad a_1 = \frac{\delta y(t_e) - \delta y(t_0)}{t_e - t_0} \tag{22}$$

and

$$b_0 = \delta z(t_0), \qquad b_1 = \frac{\delta z(t_e) - \delta z(t_0)}{t_e - t_0} \tag{23}$$

respectively. The a_1 and b_1 terms give the constant across-track and radial components of the velocity adjustment vector. Applying Eqs. (7) and (3), we can estimate improved state vectors for short time intervals like $t \in [t_0, t_e]$. By utilizing Eq. (18), we can estimate the error baseline vector $\mathbf{n}$ with

$$\begin{aligned}\mathbf{n}_{12} &= (\mathbf{r}_2^{\text{lsq}} - \mathbf{r}_1^{\text{lsq}}) - (\mathbf{r}_2^{\text{prior}} - \mathbf{r}_1^{\text{prior}}) \\ &= \mathbf{B}^{\text{lsq}} - \mathbf{B}^{\text{prior}} \simeq \Delta(\delta\mathbf{r}_{12})\end{aligned} \tag{24}$$

which shows that the estimated error vector $\mathbf{n}_{12}$ approximates the true error vector $\Delta(\delta\mathbf{r}_{12})$ according to Eq. (9). The term $\mathbf{B}^{\text{lsq}}$ denotes the improved and $\mathbf{B}^{\text{prior}}$ the prior baseline estimate.

5 Results

First, we calculate the five interferograms using the prior short-arc orbit estimates containing 10 interpolated state vectors for an interval of 45 s. Although the SAR data were acquired on different days, the acquisition starting time t_0 of each day is nearly the same for all passes. To ensure a complete correlation of both SAR images the short time interval must be chosen in such a way that it includes both the acquisition interval ($\sim$ 17 s) of the first pass and that of the second pass. To create and interpolate the 10 state vectors with the 4.5-s time intervals, we apply a Lagrange approach of 14th order and use the original orbit files containing state vectors with 60-s time intervals. We start by counting the fringes along the two distance directions because the across-track error is supposed to be greater than the radial one and causes a higher fringe gradient along distance. Next we estimate the $\delta y(t)$ components and add them to the prior state vectors. Then, we recalculate all five interferograms using the partially corrected short-arc orbit estimates before counting the remaining orbital fringes perpendicular to the track. Finally, we estimate the $\delta z(t)$ components and add the complete adjustment to the prior state vectors. This two-step process enables a more reliable and accurate fringe counting and avoids confusion with other fringes, especially in the azimuth direction. The measured fringe counts for each pair are listed in Table 2.

To evaluate the uncertainty, we first assume an a priori standard deviation of 0.1 fringes or 2.8 mm for each measurement of the fringe count. For simplicity, we assume a diagonal data covariance matrix, although measurements in pairs sharing a common image are correlated. Next, we propagate errors according to Eq. (17) to calculate the parameter covariance matrix

$$\mathbf{C}(\mathbf{x}^{\mathrm{lsq}}, \mathbf{x}^{\mathrm{lsq}}) = (\mathbf{A}^T\mathbf{W}\mathbf{A})^{-1}, \qquad \mathbf{C} \in \mathbb{R}^{n\times n} \tag{25}$$

whose diagonal elements yield the standard deviation

$$\sigma(x_j^{\mathrm{lsq}}) = \sqrt{\mathbf{C}(x_j^{\mathrm{lsq}}, x_j^{\mathrm{lsq}})} \tag{26}$$

of the adjustment component x_j^{lsq}. The numerical values of the components and their standard deviations are given in Table 3 for all six estimates. The mean values of the across-track and radial standard deviations are 2.4 cm and 4.5 cm, respectively, for the improved estimates.

Table 4 summarizes the calculated baseline components derived from the prior and improved state vectors. To estimate the error at t_0 according to Eq. (24), we use an independent program of the InSAR processing software. We can now estimate the orientation of the error vector **n** with

$$\begin{aligned} \beta &= \arccos\left(\frac{n_h}{|\mathbf{n}|}\right) \quad n_v \geq 0 \\ \beta &= -\arccos\left(\frac{n_h}{|\mathbf{n}|}\right) \quad n_v < 0 \end{aligned} \tag{27}$$

where β denotes the angle between the error vector and its horizontal component, as sketched in Fig. 5B.

The standard deviations σ_{B_h} and σ_{B_v} of the horizontal and vertical baseline components are

$$\begin{aligned} \sigma_{B_h} &= \sqrt{\sigma^2(y_1^{\mathrm{lsq}}) + \sigma^2(y_2^{\mathrm{lsq}})} \\ \sigma_{B_v} &= \sqrt{\sigma^2(z_1^{\mathrm{lsq}}) + \sigma^2(z_2^{\mathrm{lsq}})} \end{aligned} \tag{28}$$

The resulting error parameters for each interferometric pair are listed in Table 5.

We can use our improved estimates to measure the error in the prior DEOS estimates. Accordingly, we calculate the RMS value of the $n = 12$ across-track and radial correction components with

$$x_{\mathrm{rms}} = \frac{1}{n}\sqrt{\sum_{j=1}^{n}(x_j^{\mathrm{lsq}} - \bar{x})^2} \tag{29}$$

where the mean value $\bar{x}$ is zero because of Eqs. (19) and (20), respectively. This reveals 7.3 cm for the across-track and 2.4 cm for the radial component. These values are below those of Scharroo and Visser (1998), who claim RMS orbit differences of 15 cm in the across-track and 4 cm in the radial direction of the DEOS orbit solutions.

6 Discussion

Finally, we create the five post-fit interferograms using the fully corrected, short-arc orbit estimates. To improve the signal-to-noise ratio, a 2-D weighted power spectrum filter (Goldstein and Werner 1998) is applied to each interferogram. In Fig. 6, we compare the post-fit interferograms to the pre-fit ones. All post-fit interferograms show very small long-wavelength gradients, validating our new orbital tuning approach.

In order to study post- and inter-seismic deformation fields, we have recalculated pairs (10063E1, 5554E1) and (20427E1, 10063E1) in the geocoded DEM geometry using the improved orbit estimates. We are now able to do the same for the (3259E2, 10063E1) pair which spans almost 3 years and includes inter-seismic deformation of geophysical interest. This pair spans a very long time interval, but was not used in our adjustment. We compare our new orbital tuning approach with the old one of a ramp removal (Massonnet and Feigl 1998). The results are shown in Fig. 7.

The later post-seismic interferogram of pair (10063E1, 5554E1) was first calculated by Massonnet et al. (1993). It was made by differencing two co-seismic interferograms, the first composed of images acquired on 24 April 1992 and 7 August 1992 (Massonnet et al. 1993) and the second composed of images acquired on 24 April 1992 and 18 June 1993 (Massonnet et al. 1994).

Table 2. Measured interferometric fringe counts N in distance (at times t_0 and t_e) and azimuth (at NR and FR) obtained from the five interferometric pairs

Pair	$N_D(t_0)$	$N_D(t_e)$	$N_A(NR)$	$N_A(FR)$
2, 1	−1.667	1.667	1.000	−1.000
3, 2	−0.833	0.833	0.333	−0.333
4, 3	2.167	−1.500	−1.000	0.333
5, 4	−2.500	2.000	1.333	−0.833
6, 5	1.167	−1.333	0.000	0.166

Table 4. Baseline components at t_0 obtained from the DEOS orbit pairs with prior and improved estimates

Pair	B_h^{prior} (m)	B_v^{prior} (m)	B_h^{lsq} (m)	B_v^{lsq} (m)
2, 1	73.25	−14.25	73.67	−14.27
3, 2	−50.70	12.14	−50.50	12.15
4, 3	−04.96	−17.26	−05.50	−17.49
5, 4	86.59	−77.66	87.21	−77.48
6, 5	11.87	132.88	11.58	132.94

Table 3. Estimated orbit adjustment components and their standard deviations in meters at t_0 and t_e

i	$y(t_0) \pm \sigma_y$ (m)		$z(t_0) \pm \sigma_z$ (m)		$y(t_e) \pm \sigma_y$ (m)		$z(t_e) \pm \sigma_z$ (m)	
1	−0.375	0.031	−0.030	0.058	−0.413	0.031	−0.062	0.058
2	0.042	0.023	−0.045	0.043	0.007	0.023	−0.044	0.043
3	0.250	0.018	−0.050	0.034	0.216	0.018	−0.042	0.034
4	−0.292	0.018	0.181	0.034	−0.160	0.018	0.169	0.034
5	0.333	0.023	−0.001	0.043	0.342	0.023	0.019	0.043
6	0.042	0.031	−0.055	0.058	0.007	0.031	−0.037	0.058

Table 5. Error parameters at t_0 obtained from the DEOS orbit pairs with prior and improved estimates

Pair	$\|\mathbf{n}\|$ (m)	n_h (m)	n_v (m)	β (°)	σ_{B_h} (m)	σ_{B_v} (m)
2, 1	0.42	0.42	−0.02	−2.7	0.039	0.072
3, 2	0.20	0.20	0.01	2.9	0.029	0.054
4, 3	0.59	−0.54	−0.23	−156.2	0.025	0.048
5, 4	0.65	0.62	0.18	17.5	0.029	0.054
6, 5	0.30	−0.29	0.06	165.2	0.039	0.072

Figure 7a shows the immediate interferogram calculated with our improved estimates of orbits 10063E1 and 5554E1 and the corresponding SAR acquisitions.

Our improved interferograms show the geophysical deformation more clearly than previous studies. In particular, the post-seismic deformation around the northern third of the Landers rupture zone (Fig. 7j) stands out prominently. Although we believe that this signature reflects a poro-elastic effect (Peltzer et al. 1996, 1998), detailed modeling is beyond the scope of this paper. Similarly, the fringes created by the small thrust aftershock of 4 December 1992 (Fig. 7k) are now distinct from the parallel fringes to the northeast of its epicenter, which presumably recorded (mostly) the co-seismic deformation from the Landers main shock combined with (some) orbital effects (Feigl et al. 1995).

7 Conclusions

Our new orbital filtering approach can significantly improve precise orbit estimates of short arcs of ERS trajectories in an absolute sense by using interferograms as measurements of relative position. It can replace the 'Planar Orbital Tuning' post-processing algorithm (Massonnet and Feigl 1998) and might be a useful technique for assessing the quality of precise orbit products obtained from conventional POD methods. Our quasi-absolute approach is, however, restricted to those orbital passes in which SAR data were acquired. Our technique is also limited to determining the across-track and radial components of the orbital trajectory. Nevertheless, we could use timing errors, for example, to estimate the along-track error (Massonnet and Vadon 1995) and thus to estimate the complete state vectors.

Another limitation comes from the need to measure the fringe gradient accurately, a task which becomes difficult or impossible when the correlation breaks down. Such 'temporal decorrelation' occurs over wet, vegatated, or other rapidly changing surfaces. Even in good conditions like those shown here, the fringes

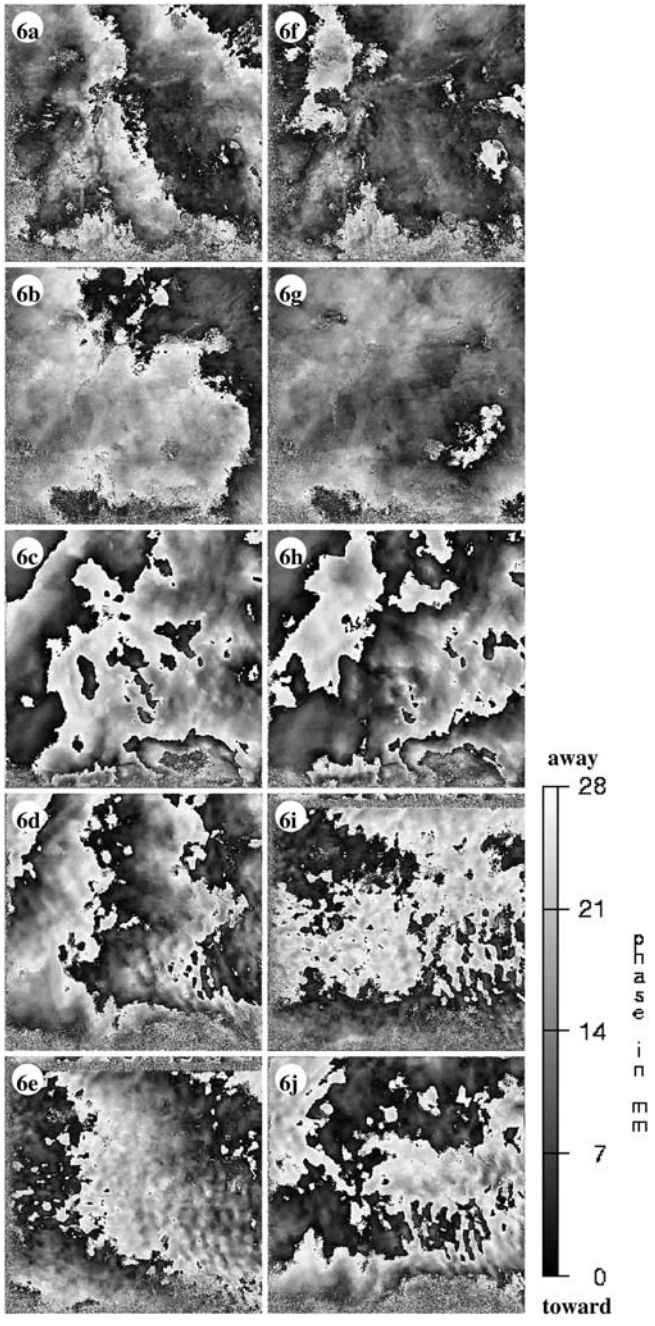

Fig. 6. Plate showing the five pre-fit (left column) and post-fit (right column) interferograms in SAR geometry caculated with the six prior and improved DEOS orbit estimates. One black-to-white scale corresponds to one interferometric phase cycle (0, 2π or to (0, 28 mm) of change in the range between the SAR antenna and a reflector on the ground. The fringe count from black to white is positive. In the left column (**b**–**e**), we clearly see orbital fringes overlapping with atmospheric artefacts in the bottom of the scene where the San Bernardino Mountains (SBM) cause rapidly changing tropospheric conditions. In **c** ($\Delta t = 35$ days), the atmospheric contribution seems to be very strong. In the right column (**f**–**j**), we find the remaining fringes after applying our new orbital tuning approach. Figure **g**–**i** confirm the strong atmospheric contributions at and around the SBM. These artefactual fringes remain after having tuned our orbital adjustments. The topographic contribution of pair (20928E1, 20427E1) (**c**) with $\varepsilon/h_a \simeq 0.04$ fringe is negligible, whereas the ones of the remaining pairs have a small influence

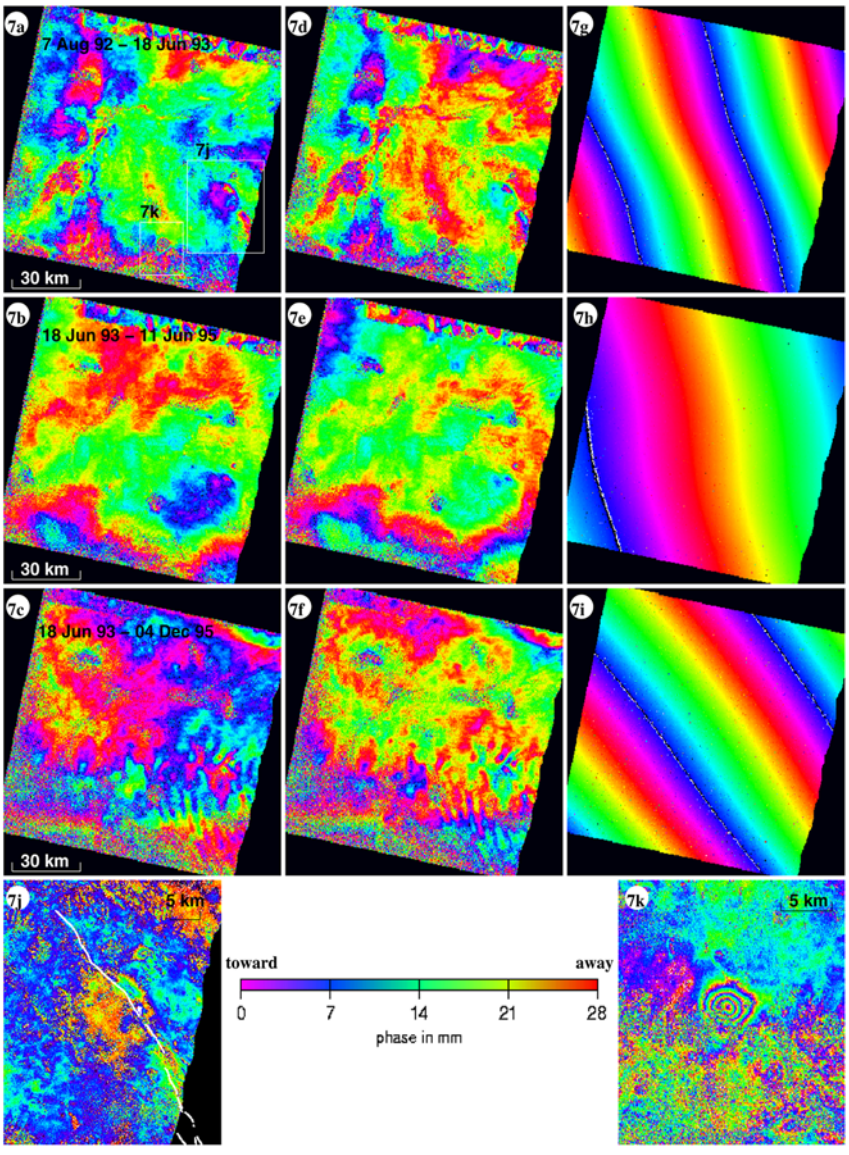

Fig. 7a-k. Plate showing post-fit interferograms of post- and inter-seismic deformation fields in DEM geometry after the Landers main shock on 28 June 1992. In this figure, one cycle of colour corresponds to one interferometric phase cycle. In the left column (**a**–**c**), we see the ones after applying our new orbital tuning approach. In those of the middle column (**d**–**f**), we see the results after applying a conventional orbital tuning approach (Massonnet and Feigl 1998). Those of the right column (**g**–**i**) show the orbital fringe residual of phase differences from the interferograms calculated with the prior and improved orbital estimates. **j** and **k** show the zooming in of the post-seismic area delimited by the white rectangles in **a**, where we have to account for a topographic error of about 7 mm. The *bold white lines* in **j** indicate the trace of the co-seismic Landers rupture as mapped in the field (Sieh et al. 1993)

become difficult to count in interferograms spanning time intervals longer than two years (see Fig. 7c and f).

Furthermore, the technique requires additional care for co-seismic or co-eruptive cases, where the deformation field can cover the entire image. In this case, we must distinguish orbital fringes from deformational fringes, for example by using a separate model to parameterize the latter (Feigl et al. 2002). Similarly, tropospheric fringes spread over long distances can resemble orbital fringes, as in the pair (20427E1, 20928E1) (see Fig. 6c).

Previous estimates of the ERS orbits are generally 'global' measures, since they are based on laser tracking and altimetric data. In areas without such data (e.g., Central Asia or the polar regions), their accuracy is likely to be degraded. Our estimates, based on local measurements of fringe gradients under short arcs, are likely to also depend on location. In this context, another validation test would be to select ERS orbit estimates for which ample tracking data exist. We could then compare locally over a test site the range calculated from newly estimated parameters with the range measured by laser tracking. Unfortunately, we have not found enough laser tracking data for the six orbits to perform a reliable error estimate.

Using our new approach to improve ERS trajectories, we can nearly eliminate orbital fringes in interferograms of post- and inter-seismic time intervals spanning more than one year. This permits us to measure inter-seismic strain fields of about 0.1 mm/km per yr and range change gradients of about 0.3 mm/km. Gradients smaller than this value tend to drown into the noise of topographic contributions or orbital residuals ($\sim$ 0.1 fringes). Applying a high-resolution DEM with an accuracy of better then 10 m would decrease the noise from topographic artefacts, thereby improving the SNR of interferograms for the study of inter-seismic or inter-eruptive deformation fields.

Acknowledgments. The authors would like to thank Gunther Kohlhammer from the ESA Research Institute (ESRIN) for his kind help in providing the ERS data held by the ESA, which holds

the copyright. They also thank Hélène Vadon from the Centre National d'Etudes Spatiales (CNES) for helpful discussions. Helpful comments from two anonymous reviewers clarified the manuscript. The first author gratefully acknowledges postdoctoral fellowships from the ESA and the Deutsche Forschungsgemeinschaft (DFG). The InSAR processing software DIAPASON was developed at CNES and licensed for use by GDR InSAR. Figures 1, 7j, and 7k were prepared using the public domain GMT software (Wessel and Smith 1998).

References

Feigl KL, Sergent A, Jacq D (1995) Estimation of an earthquake focal mechanism from a satellite radar interferogram: application to the December 4, 1992, Landers aftershock. Geophys Res Lett 22:1037–1048

Feigl KL, Sarti F, Vadon H, McClusky S, Ergintav S, Durand P, Bürgmann R, Rigo A, Massonnet D, Reilinger R (2002) Estimating slip distribution for the Izmit mainshock from coseismic GPS, ERS-1, RADARSAT, and SPOT measurements. Bull Seism Soc Am 92:138–160

Gatelli F, Monti Guarnieri A, Parizzi F, Pasquali P, Prati C, Rocca F (1994) The wavenumber shift in SAR interferometry. IEEE Trans Geosci Rem Sens 32(4):855–865

Goldstein RM, Werner CL (1998) Radar interferogram filtering for geophysical applications. Geophys Res Lett 25(21):4035–4038

Hanssen RF (2001) Radar interferometry: data interpretation and error analysis. Kluwer Academic, Dordrecht

Koch KR (1999) Parameter estimation and hypothesis testing in linear models. Springer, Berlin Heidelberg New York

Massonnet D, Feigl K (1998) Radar interferometry and its applications to changes in the Earth's surface. Rev Geophys 36:441–500

Massonnet D, Rabaute T (1993) Radar interferometry: limits and potential. IEEE Trans Geosci Rem Sens 31(2):455–464

Massonnet D, Vadon H (1995) ERS-1 Internal clock drift measured by interferometry. IEEE Trans Geosci Rem Sens 401–408

Massonnet D, Rossi M, Carmona C, Adragna F, Peltzer G, Feigl K, Rabaute T (1993) The displacement field of the Landers earthquake mapped by radar interferometry. Nature 364:138–142

Massonnet D, Feigl KL, Rossi M, Adragna F (1994) Radar interferometric mapping of deformation in the year after the Landers earthquake. Nature 369:227–230

Massonnet D, Thatcher W, Vadon H (1996) Detection of postseismic fault zone collapse following the Landers Earthquake. Nature 382:612–616

Montenbruck O, Gill E (2000) Satellite orbits: models, methods, and applications. Springer, Berlin Heidelberg New York

Peltzer G, Rosen P, Rogez F, Hudnut K (1996) Postseismic rebound in fault step-overs caused by pore fluid flow. Science 273:1202–1204

Peltzer G, Rosen P, Rogez F, Hudnut K (1998) Poroelastic rebound along the Landers 1992 earthquake surface rupture. J Geophys Res 103(B12):30 131–30 145

Scharroo R, Visser P (1998) Precise orbit determination and gravity field improvement for the ERS satellites. Geophys Res Lett 103:8113–8127

Schwarz HR (1997) Numerische Mathematik. Teubner, Stuttgart

Sieh K et al. (1993) Near-field investigations of the Landers earthquake sequence, April to July, 1992. Science 260:171–176

US Geological Survey (1993) Digital elevation models: data users guide. US Government Printing Office, Washington, DC

Wessel P, Smith WHF (1998) New, improved version of generic mapping tools released. EOS Trans. Am Geophs Un 79:579

Zebker HA, Rosen PA, Goldstein RM, Gabriel A, Werner CL (1994) On the derivation of coseismic displacement fields using differential radar interferometry: the Landers earthquake. J Geophys Res 99:19 617–19 634